PAPER • **OPEN ACCESS**

Comparison study on hyaline cartilage versus fibrocartilage formation in a pig model by using 3D-bioprinted hydrogel and hybrid constructs

Biofabrication

PAPER

Comparison study on hyaline cartilage versus fibrocartilage formation in a pig model by using 3D-bioprinted hydrogel and hybrid constructs

Hamed Alizadeh Sardroud[1,*], **Gustavo Dos Santos Rosa**[2,3], **William Dust**[4], **Tat-Chuan Cham**[2], **Gwen Roy**[5], **Sarah Bater**[6], **Alan Chicoine**[2], **Ali Honaramooz**[2], **Xiongbiao Chen**[1,7,*] and **B Frank Eames**[1,8,*]

[1] Division of Biomedical Engineering, College of Engineering, University of Saskatchewan, Saskatoon, SK, Canada
[2] Department of Veterinary Biomedical Sciences, Western College of Veterinary Medicine, University of Saskatchewan, Saskatoon, SK, Canada
[3] Department of Veterinary Surgery and Animal Reproduction, Regenerative Medicine Lab, School of Veterinary Medicine and Animal Science, São Paulo State University (UNESP), Botucatu, Brazil
[4] Division of Orthopedics, Royal University Hospital, University of Saskatchewan, Saskatoon, SK, Canada
[5] Department of Veterinary Pathology, Western College of Veterinary Medicine, University of Saskatchewan, Saskatoon, SK, Canada
[6] Department of Small Animal Clinical Sciences, Western College of Veterinary Medicine, University of Saskatchewan, Saskatoon, SK, Canada
[7] Department of Mechanical Engineering, College of Engineering, University of Saskatchewan, Saskatoon, SK, Canada
[8] Department of Anatomy, Physiology, and Pharmacology, University of Saskatchewan, Saskatoon, SK, Canada
* Authors to whom any correspondence should be addressed.

E-mail: hamed.alizadeh@usask.ca, xbc719@mail.usask.ca and b.frank@usask.ca

OPEN ACCESS

RECEIVED
16 June 2024

REVISED
26 August 2024

ACCEPTED FOR PUBLICATION
18 October 2024

PUBLISHED
5 November 2024

Keywords: hydrogel, hybrid, hyaline cartilage, fibrocartilage, synchrotron imaging, *in vivo*

Supplementary material for this article is available online

Abstract

Cartilage tissue engineering (CTE) with the help of engineered constructs has shown promise for the regeneration of hyaline cartilage, where fibrocartilage may also be formed due to the biomechanical loading resulting from the host weight and movement. Previous studies have primarily reported on hyaline cartilage formation *in vitro* and/or in small animals, while leaving the fibrocartilage formation undiscovered. In this paper, we, at the first time, present a comparison study on hyaline cartilage versus fibrocartilage formation in a large animal model of pig by using two constructs (namely hydrogel and hybrid ones) engineered by means of three-dimensional (3D) bioprinting. Both hydrogel and hybrid constructs were printed from the bioink of alginate (2.5%) and ATDC5 cells (chondrogenic cells at a cell density of 5×10^6 cells ml^{-1}), with the difference in that in the hybrid construct, there was a polycaprolactone (PCL) strand printed between every two bioink strands, which were strategically designed to shield the force imposed on the cells within the bioink strands. Both hydrogel and hybrid constructs were implanted into the chondral defects created in the articular cartilage of weight-bearing portions of pig stifle joints; the cartilage formation was examined at one- and three-months post-implantation, respectively, by means of Safranin O, Trichrome, immunofluorescent staining, and synchrotron radiation-based (SR) inline phase contrast imaging microcomputed tomography (inline-PCI-CT). Glycosaminoglycan (GAG) and collagen type II (Col II) secretion were used to evaluate the hyaline cartilage formation, while collagen type I (Col I) was used to indicate fibrocartilage given that Col I is low in hyaline cartilage but high in fibrocartilage. Our results revealed that cartilage formation was enhanced over time in both hydrogel and hybrid constructs; particularly, the hydrogel construct exhibited more cartilage

formation at both one- and three-months post-implantation, while hybrid constructs tended to have less fibrocartilage formed in a long time period. Also, the result from the inline-PCI-CT revealed that the inline-PCI-CT was able to provide not only the information seen in other histology images, but also high-resolution details of biomaterials and regenerating cartilage. This would represent a significant advance toward the non-invasive assessment of cartilage formation regeneration within large animal models and eventually in human patients.

1. Introduction

Articular cartilage may lose its structure and function over time due to the age-related wear and tear, sports injuries, diseases, and trauma [1]. Injured articular cartilage is unable to heal spontaneously in adult animals and humans [2], and further progression of articular cartilage degeneration leads to osteoarthritis, a chronic joint disorder [3]. The current treatments for severely damaged articular cartilage include the total joint replacement [4], autochondrocyte or xenochondrocyte transplantation [5], mesenchymal stem cell injection [6], microfracture [7], cartilage scraping via arthroscope [8], and transplantation of periosteum [9]. However, these treatments do not result in long-lasting healing and even need a secondary surgery later [3, 10]. Also, the tissue regenerated is typically of fibrocartilage or fibrous one rather than hyaline cartilage [11]. Hyaline cartilage contains round chondrocytes within a dense extracellular matrix (ECM) mainly composed of glycosaminoglycans (GAGs) and collagen type II (Col II) [12]; while fibrocartilage contains densely-packed, elongated chondrocytes within an ECM of abundant collagen type I (Col I) and is featured by the inferior mechanical properties, leading to the reduced articular cartilage functions as compared to hyaline cartilage [13].

Promising articular cartilage therapies focus on cartilage tissue engineering (CTE), which uses engineered constructs to help regenerate new cartilage. Among them, hydrogel-based constructs have garnered attention [14] due to their ability to incorporate chondrocytes while maintaining their morphology and phenotype [15]. Static culture of hydrogel constructs *in vitro* has shown that incorporated cells can produce hyaline cartilage ECM as indicated by the examination of GAGs and Col II, as well as low fibrocartilage regeneration as indicated by Col I [16]. However, static *in vitro* culture does not replicate the biomechanical conditions of native cartilage *in vivo*, which can result in different cellular responses when hydrogel constructs are implanted. This dichotomy may result in the outcome disconnect between *in vitro* and *in vivo* [17]. Unfortunately, most *in vivo* studies examined only the formation of GAGs and Col II at the sites of cartilage defects (where the constructs were implanted), but not investigated into the potential fibrocartilage formation [13, 18]. Furthermore, the *in vivo* studies have primarily performed on small animal models [19, 20], such as rabbits that do not replicate the biomechanical conditions of larger animals or humans. Also, previously studies have indicated that the fibrocartilage formation in the hydrogel-based methods may be of an issue due to the biomechanical forces [21–23] emphasizing the need for CTE approaches to assess fibrocartilage formation under mechanical load [17].

In this study, we hypothesized that the excessive mechanical forces exerted on the cells within engineered constructs promote the fibrocartilage formation at the knee joints. To test this hypothesis, we employed the state-of-the-art three-dimensional (3D)-bioprinting technique to fabricate alginate/-polycaprolactone (PCL) hybrid constructs and alginate-alone constructs (both with living cells) and then investigated into the formation of hyaline cartilage and fibrocartilage. We strategically designed the hybrid constructs by employing the force-shielding mechanism to reduce the forces on the cells within the alginate hydrogel strands, which were printed in the spaces or canals between the printed PCL strands (figure 1(B)) [13]. Previous studies have illustrated that the cells within such hybrid constructs remain highly viable and are able to secrete GAGs and Col II *in vitro* [24–26]. In the current study, both hydrogel and hybrid constructs were implanted into the stifle (knee) joints of pigs and underwent both qualitative and quantitative analyses on the hyaline cartilage vs. fibrocartilage formation. In addition to standard histological stains and biochemical assays to characterize cartilage ECM formation, Col I and Col II deposition were assessed quantitatively to determine whether the new-generated tissue was of hyaline cartilage or fibrocartilage.

Cartilage regeneration has been typically evaluated *in vivo* using traditional, yet invasive, techniques that provide only 2D assessments of 3D tissue regeneration, limiting the visualization of spatial outcomes [27]. Notably, these traditional techniques like biochemical assays and histological analysis require sample excision, obscuring spatial information and necessitating large animal use, which is costly and raises ethical concerns [26, 28–30]. Most importantly, all of these approaches have to be relinquished

with the advance from animal to human studies; and non-invasive imaging techniques must be developed and used for examining the constructs and tissue regeneration at intermediate times during the repair process. Non-invasive imaging techniques, such as micro-computed tomography (micro-CT) or magnetic resonance imaging (MRI) are able to offer valuable 3D insights into the structural characteristics of implanted tissue constructs without the need for invasive procedures [31–33]. Notably, these imaging techniques have limited or poor contrast and spatial resolution for characterizing the implanted constructs within newly-formed and surrounding native tissues [34, 35]. With the advance of synchrotron light, new non-invasive imaging techniques have emerged in the fields of biomedical and material sciences [36]; among these techniques, the synchrotron radiation (SR)-based inline phase contrast imaging microcomputed tomography (inline-PCI-CT) shows the most promising [37, 38]. Inline-PCI-CT utilizes phase shift variations in x-rays passing through samples to visually distinguish each material and tissue that has a different refractive index [39, 40]. The potential of inline-PCI-CT to assess fabricated constructs and their time-dependent structural changes has been demonstrated both *in vitro* and *in vivo* [30, 41, 42]. In this study, we utilized inline-PCI-CT to visualize implant components and monitor regeneration in a large animal model, comparing these results with traditional histological sections to identify cartilaginous features.

2. Materials and methods

2.1. 3D bioprinting hydrogel and hybrid constructs

A-cell-alginate mixture was prepared using a well-established *in vitro* chondrogenic cell line from mice, ATDC5 [43], as previously described [44]. Briefly, ATDC5 cells from RIKEN cell bank (Japan) were cultured in Dulbecco's modified Eagle's medium/Ham's nutrient mixture F12 (DMEM/F12, Sigma, D8900, USA) supplemented with 5% fetal bovine serum (FBS, Gibco, USA) and 1% penicillin/streptomycin (Sigma, USA). The cells were trypsinized at confluency and mixed with alginate solution at a final cell density and alginate concentration of 5×10^6 cells ml^{-1} and 2.5%, respectively. The resulting mixture was used as a bioink for bioprinting both hydrogel and hybrid constructs on a 3D-Bioplotter (Envisiontec, Germany) (figure 1(A)).

Alginate bioink was printed through a 200 μm conical needle into a 6-well plate containing 50 mM calcium chloride solution ($CaCl_2$, Sigma-Aldrich) layer-by-layer, forming the hydrogel construct with a cylindrical shape with a diameter of 8 mm and a height of 2 mm. This height was designed according to the *in vivo* conditions, where articular cartilage in pig joints has 1.5–2 mm thickness [45, 46]. The fabricated constructs were then transferred to another well with DMED-F12 media and were rinsed twice with media.

Hybrid constructs were fabricated as per the previously established protocol [25]. Briefly, PCL beads (Sigma-Aldrich, Mw 48 000-90 000) were loaded into a high temperature printing head of the 3D-Bioplotter, melted, and maintained at 65 °C–80 °C for 15–20 min before printing to kill any microbial contamination. The PCL strands were printed at 80 °C through a cylindrical metal needle with an inner diameter of 300 μm on a printing stage with a temperature controlled at 10 °C. The cell-impregnated alginate bioink strands were printed through a conical needle with an inner diameter of 200 μm. The deposition of PCL and bioink strands was done in an alternating manner, ensuring a 1 mm gap between PCL–PCL strands and between bioink–bioink strands. This strategy aimed to strategically design the hybrid constructs by employing the force-shielding mechanism to alleviate the forces on the cells within the alginate hydrogel strands, which were printed in the spaces or canals between the PCL strands. Additionally, the strands in adjacent layers were oriented at 0° and 90° angles alternately. Overall, hybrid constructs had a cylindrical shape with a diameter of 8 mm and six layers in height, about 2 mm. During fabrication, 170 mM $CaCl_2$ aerosol released from a nebulizer (MY-520) was used to conduct partial cross-linking. In order to further crosslink the alginate strands, the fabricated constructs were submerged in a 100 mM $CaCl_2$ solution for 20 min. Then, the constructs were rinsed twice in DMEM/F12 solution for 5 min.

The fabricated hydrogel and hybrid constructs were transferred immediately to a media consisting of differentiation medium: DMEM/F12 supplemented with 5% FBS, 1% penicillin/streptomycin, 10 mg ml^{-1} insulin-transferrin-selenium (ITS, Sigma, I3146), and 0.05 mg ml^{-1} ascorbate-2-phosphate (Sigma, A8960). The 3D-bioprinted constructs were cultured inside a 37 °C incubator with 5% CO_2 for 10 d prior to implantation, to initiate chondrogenic differentiation of the cells. Differentiation media was changed every other day.

2.2. *In vivo* implantation of hydrogel and hybrid constructs

Pigs were selected for these *in vivo* experiments since their joint conditions resemble human joints in terms of gross anatomy, size, weight application, and cartilage thickness [47], along with the fact that the biomechanicsl conditions at the pig joints are similar to human joints. All animal protocols were approved by the Animal Research Ethics Board of the University Animal Care Committee from

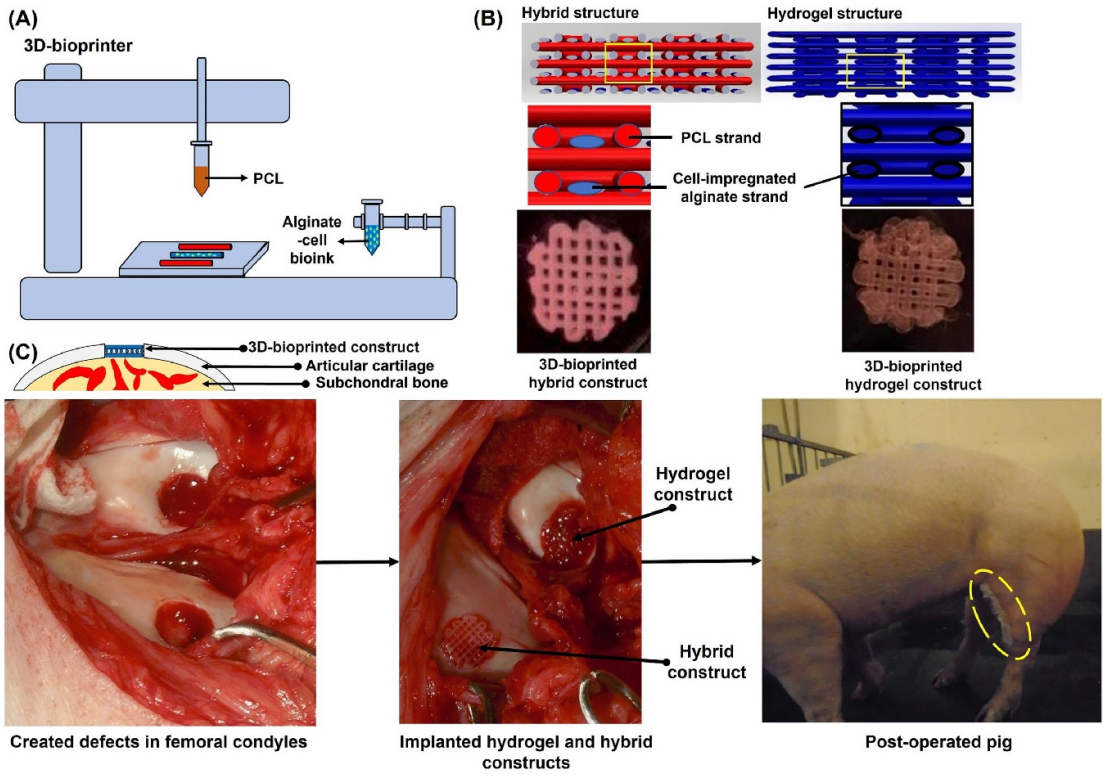

Figure 1. Fabrication of constructs and their implantation into a pig model. (A) Hydrogel and hybrid constructs were fabricated on a 3D-bioprinter. (B) Hydrogel constructs (right) were composed of cell-impregnated alginate strands alone, while hybrid constructs (left) were composed of both cell-impregnated alginate strands and PCL. Note that cell-impregnated alginate strands are not as tall as PCL strands, thus shielding the cells from the force or stress. (C) Cylindrical defects were created in the femoral condyles of pigs (left) and then treated with 3D-bioprinted hydrogel and hybrid constructs (middle); and the treated pigs were set free to stand and walk after surgery (right).

the University of Saskatchewan (#AUP 20140091) in compliance with Canadian Council on Animal Care guidelines. Specifically, ten (10) female pigs, each about 6 months of age and weighing about 130 kg, were sourced from the Pig Improvement Company Canada (Winnipeg, MB). The surgeries and animal care before and after the surgical procedures were conducted at the Prairie Swine Centre (Saskatoon, SK). Xylazine (2.2 mg kg^{-1}; Rompun^{TM} 100 mg ml^{-1} injectable, Elanco Canada Ltd, Mississauga ON) and butorphanol (0.2 mg kg^{-1}; Torbugesic®, Zoetis Canada Inc, Kirkland QC) were combined in one syringe and administered to pigs in their holding pen by intramuscular injection (IM, behind the ear) for sedation/premedication. For general anesthesia, the pig trachea was intubated for inhalation anesthesia following intravenous injection (IV) of ketamine hydrochloride (2 mg kg^{-1}; Narketan, Vetoquinol N.-A. Inc., Lavaltrie, QC). Following intubation, the pig was moved onto a veterinary operating table, and inhalation anesthesia of Isoflurane USP (Fresenius Kabi Canada Ltd, Toronto, ON) started, with the option of administering additional ketamine boluses as needed. An IV catheter was placed for administration of 0.9% saline/norm-R/Lactated ringers (2 ml kg h^{-1}) to maintain hydration during surgery. Anesthesia monitoring was performed continually with recordings made every 5 min for heart rate and respiratory rate; temperature recordings were made at least hourly.

The left stifle (knee) was selected for each pig for implantation of the constructs (figure 1(C)). The skin over the implantation site was surgically prepared (shaved, washed, and sterilized with povidone iodine solution). A surgical incision was performed on the craniomedial aspect of the femorotibial joint, starting proximally, and extending distally over the joint. Muscle and fat tissues around the joint cavity were sharply dissected and an incision was made in the joint capsule. By physically flexing the joint and luxating the patella medially, a portion of the femoral condyle was exposed. One defect with a diameter of 8 mm and a depth of about 2 mm, reaching the surface of the subchondral bone, was created on each of the lateral and medial femoral condyles using a biopsy punch (figure 1(C)). The defects were then cleaned with forceps and small curettes, and a hydrogel or hybrid construct was implanted into each defect. Implantation sites for hydrogel and hybrid constructs were alternated (lateral or medial condyle) for each animal until the last surgery. In a preliminary study, cell-free 3D printed scaffolds were implanted into

defects in a joint of one pig. Pig's blood was collected into an anticoagulant tube, centrifuged, and the resulting platelet-rich plasma (PRP) was transferred into a sterile tube. Thrombin from bovine plasma (Sigma, T6634) was added to the PRP to activate it, followed by gentle mixing. Some of the implants were covered with activated PRP as an adhesive fibrin-like glue [48], while others were left uncovered. After two weeks, the pig was euthanized, and both types of implanted scaffolds, with and without PRP covering, remained in the defects. Based on this observation, no PRP covering was used for the subsequent surgeries to reduce the duration and extent of surgical procedures performed on the animals.

After the operated joint was returned to the normal anatomical position, sterile sutures were used to close the joint capsule and skin. The pig was given a single subcutaneous dose of buprenorphine (0.12–0.24 mg kg^{-1}) for post-operative analgesia, sourced from Chiron Compounding Pharmacy Inc in Guelph, ON, and injectable meloxicam (Metacam® 20 mg ml^{-1} Solution for Injection, Boehringer Ingelheim Animal Health Canada Inc, Burlington, ON) was administered at a dose of 0.4 mg kg^{-1} via intramuscular injection daily for 5 d post-surgery. The animals were allowed to move freely in stalls after surgery, while being subject to daily physical examinations for monitoring their recovery and overall health. After one and three months, respectively, the animals were sacrificed using a captive bolt (5 pigs per time-point).

2.3. Gross examination

After sacrificing the pigs, implanted regions were excised with a bone saw, and the femoral condyles, including the implantation sites, were photographed and examined grossly. Each defect site was examined to determine how closely the newly formed tissue resembled normal hyaline articular cartilage. The coverage, color, surface, and margins of each defect ($n = 4$) were evaluated grossly by three observers using a gross scoring system (table 1) modified from the Wayne scoring system [49]. Subsequently, each implanted construct and surrounding cartilage and bone were further excised with a bone saw and fixed in 4% paraformaldehyde (PFA) in phosphate-buffered saline on a rocker overnight at room temperature. Afterwards, the samples were dehydrated over many hours with increasing concentrations of ethanol, with the final step using 100% ethanol, and stored at −20 °C for further analyses.

Table 1. Scoring system for gross evaluation of articular cartilage defects.

Gross appearance	Grade
Coverage	
>75% fill	4
50%–75% fill	3
25%–50% fill	2
<25% fill	1
No fill	0
Neocartilage color	
>75% transparent surface	4
50%–75% transparent surface	3
25%–50% transparent surface	2
<25% transparent surface	1
0% transparent surface (Opaque surface)	0
Defect margins	
<25% circumference visible	4
25%–50% circumference visible	3
50%–75% circumference visible	2
>75% circumference visible	1
Entire circumference visible	0
Surface	
Smooth/level with normal	4
Smooth but raised	3
25%–50% irregular	2
50%–75% irregular	1
>75% irregular	0

2.4. Imaging of implanted constructs via inline-PCI-CT scanning and 3D image reconstruction

The excised samples (each comprising one defect and surrounding tissues) were transferred to the Canadian Light Source (CLS, Saskatoon, SK) and scanned by means of inline-PCI-CT at the Biomedical Imaging and Therapy beamline, as previously described ($n = 5$) [30]. Briefly, samples were secured in a sample holder and placed on a rotating stage, which was located 58 cm and 85 cm from the beam source and detector, respectively, for scanning at an imaging energy of 30 keV. Samples were rotated 180° while collecting 2000 projections on a beamline monitor (AA-60; Hamamatsu) combined with a CCD camera (PCO 4000) with an effective pixel size of 8.9 μm and scanning exposure time of 0.290 s.

The application of Paganin/transport-of-intensity phase retrieval, combined with CT reconstruction, was performed with delta/beta ratio of 300 on raw projection datasets using open-source UFO-KIT software available at CLS to produce virtual 2D image slices. The histogram was clipped based on the minimum and maximum grey values of −0.001 and 0.0015, respectively, obtained from a test reconstruction, in order to convert the reconstructed values from 32-bit to 8-bit. 2D virtual slices were used for 3D-volume rendering using either manual or automatic segmentation with Amira software (FEI, France) or a two-step process involving pre-segmentation with Amira and interpolation using the smart interpolation tool provided by the online Biomedisa platform (https://biomedisa.org) [50]. Briefly, Amira was used for manual segmentation of different components on every tenth slice. Subsequently, the online Biomedisa platform's automatic interpolation tool was utilized to interpolate and segment the remainder of the volume between the pre-segmented slices. The segmentation

results were then imported back into Amira for further refinement, where minor errors were manually corrected.

2.5. Tissue processing and sectioning

After imaging at CLS, samples were cut into smaller pieces of about 10 mm × 10 mm × 5 mm ($W \times L \times H$), encompassing the implanted constructs, adjacent cartilage, and subchondral bone. The samples were then decalcified in 19% (w/w) ethylenediaminetetraacetic acid (EDTA) in double distilled water over three weeks on a rocker at room temperature, changing solution every other day. Decalcified samples were cut into 5 equal sagittal slabs to represent the edges and center of each defect (supplemental figure 1) and then were processed in graded ethanol, xylene, and paraffin using a Leica PEARL Tissue Processor. The slabs were embedded in paraffin, and sagittal sections of 10 μm were obtained using a Leica Digital microtome. The sections were mounted on Superfrost Plus microscopy slides and stored at room temperature. Tissue processing and sectioning steps were carried out at the Histology Core Facility of the University of Saskatchewan.

2.6. Histology

Production of GAGs and collagen fibers were visualized by Safranin O/fast green and Milligan's Trichrome staining, respectively, of adjacent histological sections as previously described [51, 52]. Safranin O stains sulfated GAGs red, and fast green is a counterstain [53, 54]. Aniline blue staining of collagen fibers (usually Col I or Col II) results in a dark blue staining of bone and dentine, and a light blue staining of cartilage in the Milligan's Trichrome protocol [52]. Stained sections were imaged at 4x magnification using a light microscopy (Nikon, Eclipse E600, SPOT Insight™ Camera), and images were stitched together to cover the entire section.

2.7. Col I and Col II immunodetection

Col I and Col II immunofluorescence were performed on tissue sections to detect deposition of Col I and Col II, respectively, as previously described [44, 55]. Briefly, the sections were digested with 0.1% trypsin (MP Biomedicals) at 37 °C for 15 min, followed by treatment with 0.5% hyaluronidase (Worthington) at 37 °C for 15 min for antigen retrieval. After blocking in 4% goat serum (Sigma) and 2% sheep serum (Sigma) in PBST (0.5% Triton X-100 mixed in PBS), primary antibodies against Col I (1:100; 2150-1410, BioRad) and Col II (1:100; II-II6B, DSHB) in blocking buffer were applied overnight at 4 °C. After PBST washing, secondary antibodies of goat anti-rabbit IgG-594 (1:1000, Invitrogen) and goat anti-mouse IgG-488 (1:1000, Invitrogen) in blocking buffer were applied for 3 h in the dark at room temperature. DAPI mounting medium (Vectashield) was applied on the slides, images of the sections were taken with a fluorescence microscope (Nikon, Eclipse E600, SPOT Insight™ Camera), and images were stitched together to cover the entire section. Col I, Col II, and DAPI were visualized in red, green, and blue, respectively.

2.8. GAG and collagen image quantitation

GAG production was quantitated from images of Safranin O-stained sections using Adobe Photoshop software (Adobe systems Inc., version 13.0, San Jose, CA, USA). Margins of each defect were identified by tissue discontinuities with surrounding host tissues, in some cases assisted by evaluating Safranin O or collagen immunostaining on neighboring native cartilage, which was generally much higher than in the defect region. Photoshop's lasso tool was used to isolate the defect area based on those margins, and the number of pixels in this region was recorded as the '*regenerated tissue*'. Using the color range tool built into the software, a specific range of colors can be selected [56]. As reference for GAG deposition, a group of pixels of positive Safranin O staining was selected by applying a color range to the native cartilage, and when such a color range successfully identified native cartilage on a wide range of slides from many samples, this color range was saved for use in all analyses. The number of positive red pixels selected by this standard color range in each defect area was recorded. To reveal '*%GAGs/regenerated tissue*', data were expressed as a percentage of selected red pixels in the defect pixels.

A similar approach was used to determine the relative abundance of hyaline cartilage and fibrocartilage in defect areas of immunostained section images (supplemental figure 3). To define the Col II staining reference color range, green pixels in immunostained images were reproducibly selected from native cartilage, as described above. Application of this reference color range to isolated defect areas produced '*%New cartilage/regenerated tissue*', since Col II is high in both hyaline cartilage and fibrocartilage. To quantitate the amount of newly formed fibrocartilage, both Col I and Col II images were opened in Photoshop as layers. The Col I staining reference color range was defined by reproducibly selecting red pixels in the superficial zone of native cartilage. Then, selected Col II pixels in the defect area were used to generate a mask on the Col I images. Within this masked region, red pixels that were selected by the Col I staining reference color range would be positive for both Col I and Col II, so this represented how much of the new cartilage was fibrocartilage, or '*%fibrocartilage/new cartilage*'. Finally, the inverse of this calculation led to '*%hyaline cartilage/new cartilage*'.

For each of these quantitative assessments, samples from four different pigs were analyzed ($n = 4$). To account for regional differences within each sample across the defect area (supplemental figure 1), three adjacent slabs (out of five per sample) from the marginal region to the central region of the

defects were sectioned, and three slides per slab were stained and imaged ($n = 9$ per sample).

2.9. Terminology

Defects implanted with 3D-bioprinted hydrogel and hybrid constructs are referred as hydrogel-treated defects and hybrid-treated defects, respectively.

2.10. Statistical analysis

Statistical analyses were performed with GraphPad Prism software package version 9.4.1. As all groups had small sample sizes, non-parametric statistical Kruskal–Wallis one-way analysis of variance (ANOVA) followed by Dunn's multiple comparisons test was used. Quantitative results are presented as mean value with the corresponding standard deviation (SD) within the context, while the figures depict median and the interquartile range (IQR), and statistical significance was accepted for p values of less than 0.05.

3. Results

3.1. Gross analyses suggested that articular cartilage increased in defect-treated areas over time

Post-surgery gross images showed that cartilage defects were created in the same general region of the femoral condyles with slight varying positions (figures 2(A) and (B)). Considering that the substantial size of the femoral condyle relative to the defect size, it is reasonable to assume that both hydrogel-treated defect and hybrid-treated defect be subject to the same forces or mechanical conditions. Both hydrogel-treated defects and hybrid-treated defects were filled with regenerated tissues at both the 1 month and 3 month post-implantation timepoints (figures 2(A) and (B)). One-month after implantation, the margins of the defects remained clearly visible, with little apparent integration of new tissue with adjacent cartilage (figures 2(A)–(A″)). Likewise, little to none of the regenerated tissue appeared to have the glassy sheen that gives hyaline cartilage its name, and the surface of the defects was very irregular and not smooth, with large central depressions. For hybrid-treated defects at one-month post-implantation, PCL strands were also visible in some cases in these depressions (figure 2(A″)). Three months after implantation, the margins of both types of defects were much less visible, and the regenerated tissues were better integrated with the surrounding native cartilage (figures 2(B)–(B″)). A lot of the defect areas had a glassy, hyaline appearance, more obvious in the hydrogel-treated defects than the hybrid-treated defects. Compared to one-month, the surfaces of the defects at three-months post-implantation appeared more regular and smooth, and the depressions were less noticeable (figures 2(B)–(B″)). No evidence of acute or sustained immune reaction was observed at any time after surgery (data not shown), which might have been expected with ATDC5 mouse cells implanted in pigs, suggesting that the hydrogel shielded the impregnated cells from the host immune system. Using Wayne's gross scoring system (table 1) [49], both hydrogel-treated defects and hybrid-treated defects showed an increasing trend in total scores from one- to three-months post-implantation (figure 2(C)), indicating a possible improvement in regeneration of the new tissue. The hydrogel-treated defects had slightly higher total scores than the hybrid-treated defects at both timepoints.

3.2. Histology staining showed increased cartilage regeneration within treated defects over time

Safranin O staining was used to illustrate sulfated GAG deposition in regenerating tissue of the femoral condyle defects. Safranin O staining showed that GAG deposition increased within both hydrogel-treated defects and hybrid-treated defects over time (figure 3). One-month post-implantation, hydrogel-treated defects had large areas of Safranin O staining, while hybrid-treated defects had none (figures 3(A) and (B)). By three-months post-implantation, Safranin O staining was strong in both defects, but hydrogel-treated defects still seemed to have higher staining than hybrid-treated defects (figures 3(C) and (D)). Several Safranin O-positive cells at deeper regions of the regenerating tissue showed rounded chondrocyte morphology within lacunae (figures 3(C″), (C‴), (D″) and (D‴)) similar to what was seen in the surrounding normal hyaline cartilage (figures 3(A⁗)). Such non-integrated, regenerated hyaline cartilage was even observed in hydrogel-treated defects one-month post-implantation, mostly at neighboring regions to the native cartilage (figure 3(A‴)).

For both defects at the two timepoints, superficial regions of the regenerated tissue with less Safranin O staining showed densely-packed, elongated cells, which may simply indicate undifferentiated mesenchyme, but also could reflect formation of fibrocartilage (figures 3(A′)–(D′)) [57], similar to what was seen in the surrounding superficial zone of normal articular cartilage (figure 3(A″)). For hybrid-treated defects at 1 month post-implantation, the majority of cells throughout the regenerating tissue showed this fibroblastic appearance (figures 3(B)–(B″)). At three-months post-implantation, this feature decreased in deeper regions of the regenerating tissue for both types of defects (figures 3(C) and (D‴)).

Holes in the sections of hybrid-treated defects were likely artifacts that reflected where PCL strands used to be in the regenerating tissue before they were extracted by xylenes during histological processing (see 'P' in figures 3(B) and (D)). According to this inference, fewer PCL strands were observed in hybrid-treated defects at three-months post-implantation,

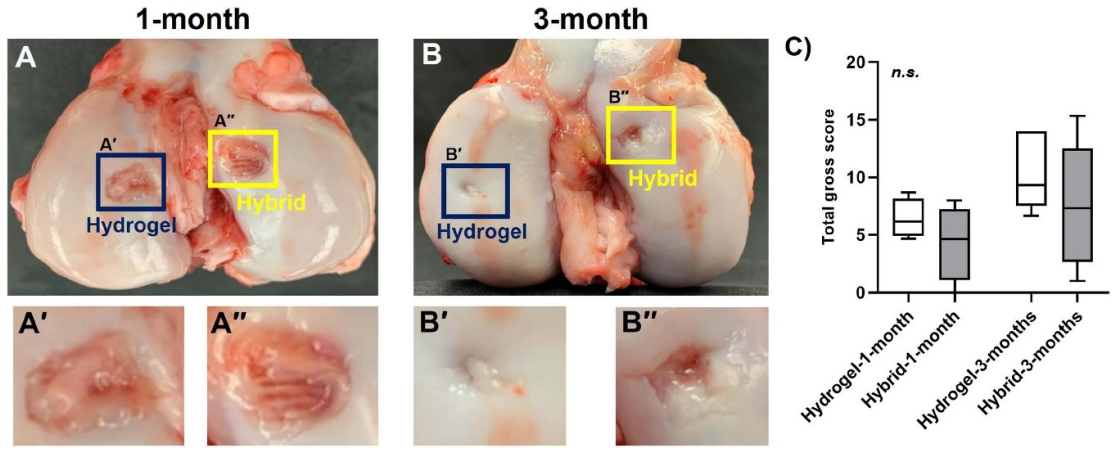

Figure 2. Gross analyses suggested that articular cartilage increased in treated defect areas over time. (A)–(B) Gross images of dissected joints one- (A), (A′), and (A″) and three-months (B), (B′), and (B″) post-implantation. Defects are marked with dark blue and yellow squares for hydrogel-treated defects and hybrid-treated defects, respectively. (C) Gross grading of the defects showed an enhanced treatment trend for both hydrogel-treated defects and hybrid-treated defects, indicating an improvement in the healing and regeneration of the joint tissue ($n = 4$ for each experimental group at each timepoint; n.s. = not significant).

and those remaining were displaced deeper into the subchondral bone (see 'P' in figure 3(D)).

Safranin O stained images were used to quantitate the area of GAGs within regenerating tissues (see Methods 3.8). The percentage of GAGs appeared to increase over time for both hydrogel-treated defects and hybrid-treated defects. In hydrogel-treated defects, Safranin O-positive pixels covered 33.0 ± 25.4% and 41.6 ± 23.8% of regenerating tissues at one- and three-months post-implantation, respectively (figure 3(E)). An increasing trend of GAG secretion was also observed in hybrid-treated defects over time, with 0.2 ± 0.2% and 22.4 ± 22.1% of regenerating tissues covered with Safranin O-positive pixels at one- and three-months post-implantation, respectively (figure 3(E)). Hydrogel-treated defects tended to have more Safranin O-positive pixels, compared to hybrid-treated treated defects at both timepoints. However, no statistically significant difference was observed between groups or timepoints (figure 3(E)). In total, Safranin O analyses verified gross observations that cartilage production increased over time in both treated defects.

Representative images from the center to the margin of both treated defects were analyzed with the results highlighting their histological differences. Safranin O staining showed significant regional variation in GAG deposition, with higher staining in the margins for both treated defects (supplemental figure 2). At both one and three months post-implantation, hydrogel-treated defects had more staining at the margins (supplemental figures 2(A)–(F)), while hybrid-treated defects had minimal staining at one month (supplemental figures 2(G)–(I)) but showed more staining at three months, though less between the center and margin (supplemental figures 2(J)–(L)). This regional analysis underscores the need for comprehensive sampling to capture general findings, as reflected in all study analyses. Aniline blue staining of Milligan's Trichrome protocol was used to illustrate fibers of collagen in regenerating tissue of the femoral condyle defects, where a higher density of those fibers gives stronger blue staining [53]. Much of the articular cartilage adjacent to the treated defects had a light blue color with rounded chondrocytes (figures 4(A), (A′′′′)), indicating the more sparse collagen fibers typical of hyaline cartilage; whereas the superficial zone of articular cartilage had slightly stronger staining with more densely-packed, elongated cells (figures 4(A), (A″)), suggesting the denser fibers typical of fibrocartilage [54]. According to these internal controls, Aniline blue staining intensity and cell morphology were used to evaluate cartilage deposition in regenerating tissue of both hydrogel-treated and hybrid-treated defects.

Trichrome staining (on sections adjacent to the Safranin O data in figure 3) indicated that cartilage collagen deposition increased over time for both treated defects (figure 4). Regenerating tissues in the hydrogel-treated defects appeared slightly blue at one-month post-implantation, while the higher magnification images revealed that most of this appearance was not due to ECM staining by Aniline blue but the clusters of cells with sparse ECM staining (figures 4(A), (A′) and (A′′′)). Darker blue staining was observed around densely-packed elongated cells in a broad region near the surface of the regenerating tissue (figures 4(A) and (A′)). In the hybrid-treated defects at one-month post-implantation, little to no light blue staining was observed throughout the regenerating tissue, but darker blue staining appeared at the surface and in a few other locations (figures 4(B), (B′) and (B″)). Regions of hyaline-cartilage-like Aniline blue staining in ECM

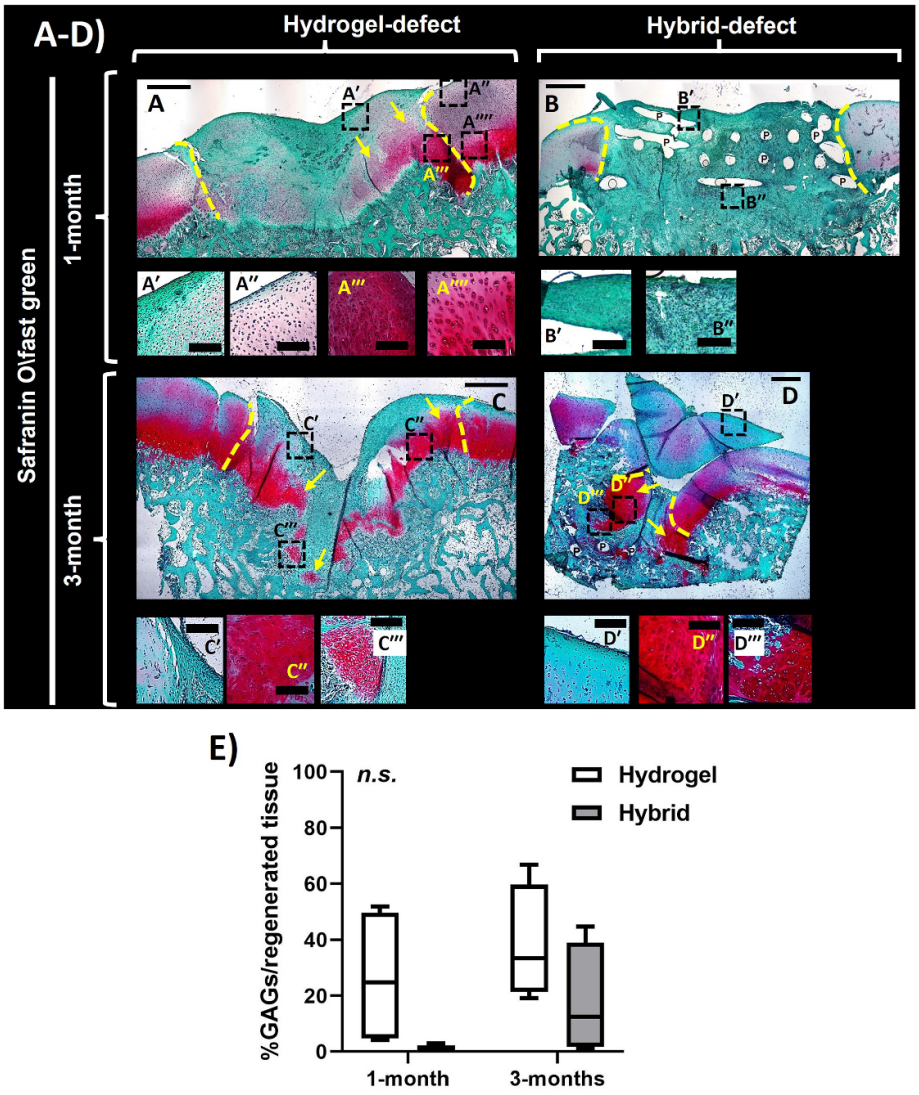

Figure 3. Safranin O staining demonstrated that GAG deposition increased over time in both treated defects. (A) Numerous Safranin O-stained regions (yellow arrows) of the regenerating tissue (within dashed yellow lines) were seen in hydrogel-treated defects at one-month post-implantation. (B) Hybrid-treated defects at one-month post-implantation showed little to no Safranin O staining in the regenerating tissue (within dashed yellow lines). (C), (D) Safranin O staining (yellow arrows) increased for both type of defects at three-months postimplantation, while less PCL strands (labelled P) were visible in hybrid-treated defects. (A′)–(A′′′), (B′)–(B′′), (C′)–(C′′′), (D′)–(D′′′)) Higher magnification views of boxed regions in panels A-D demonstrated histological staining and cell morphology in different regions of the regenerating tissue and surrounding articular cartilage. (E) Quantitation of Safranin O-stained red pixels (see Methods 3.8) showed a trend of increased GAG deposition for hydrogel-treated defects and hybrid-treated defects over time, and hydrogel-treated defects seemed to have more GAGs than hybrid-treated defects at both timepoints, although these were not statistically significant ($n = 4$ for each type of defect at each timepoint). Abbreviations: n.s. for not significant and P for PCL strands. Scale bars: A-D = 1 mm; A′-D′′′ = 200 μm.

containing round chondrocytes increased dramatically at three-months post-implantation for both defects (figures 4(C) and (D′′′)). In both treated defects at three-months, darker blue color around densely-packed, elongated cells was seen mostly at the surface and a bit in the center of regenerating tissues (figures 4(C) and (D′′′)). Both treated defects showed improvement over time in terms of integration between the regenerating tissue and surrounding native cartilage. By comparing trichrome stained images with the adjacent safranin O stained images (figure 3), regions of light blue staining were also Safranin O-positive regions, independently supporting designation of this tissue as hyaline cartilage. On the other hand, dark blue regions had little to no Safranin O staining, arguing that these tissues were fibrocartilage, other connective tissues, or undifferentiated mesenchyme.

3.3. Collagen 2 immunostaining showed increased cartilage regeneration, while Collagen 1 immunostaining showed increased fibrocartilage and fibrous tissue, at the treated defects over time

To identify the cartilage generated in the treated defects of either hyaline or fibrocartilage, we also conducted immunofluorescent staining of Col I and Col II on sections adjacent to the histology. At the hydrogel-treated defects, Col II immunostaining was

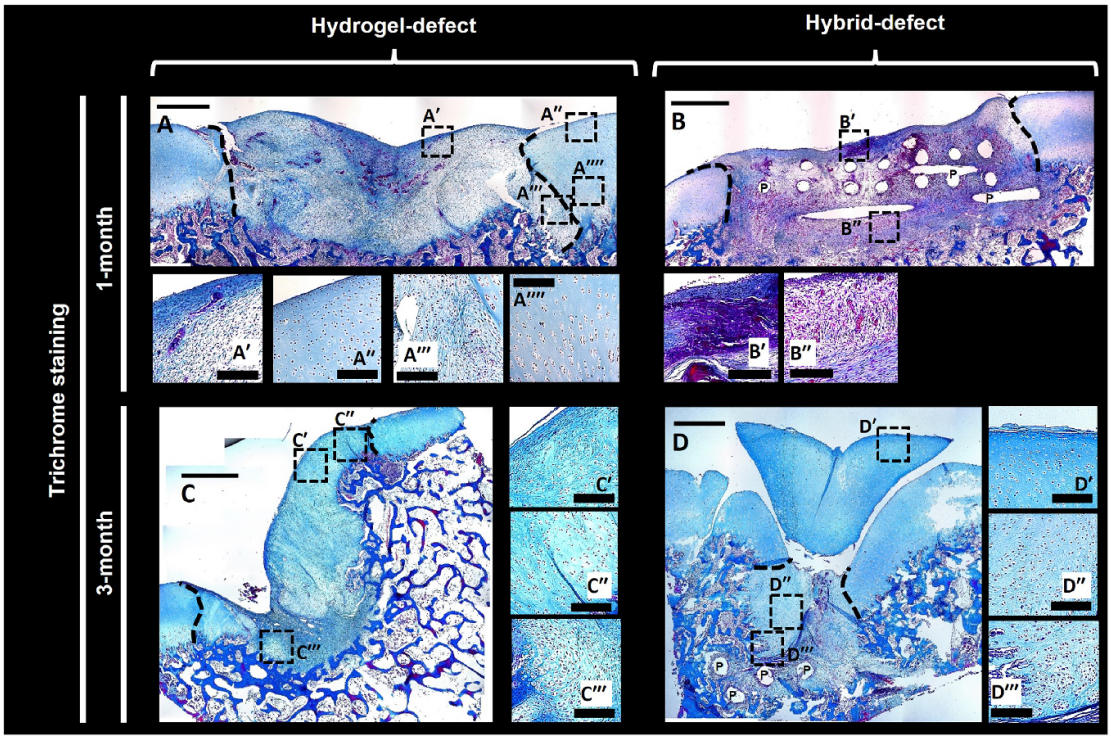

Figure 4. Trichrome staining demonstrated that hyaline cartilage-like collagen fiber deposition was increased over time in both hydrogel-treated and hybrid-treated defects. (A) Compared to surrounding articular cartilage (outside of dashed lines), hydrogel-treated defects at one-month post-implantation had more darker blue staining ECM than lightly stained ECM in regenerating tissues (within dashed lines). (B) Hybrid-treated defects at one-month postimplantation mostly had a little darker blue staining ECM near the surface of the regenerating tissue (within dashed lines). (C), (D) Collagen fibers with hyaline cartilage characteristics were observed throughout regenerating tissues at three-months post-implantation for both defects. (A′)-(A⁗), (B′)-(B″), (C′)-(C‴), (D′)-(D‴) Higher magnification views of boxed regions in panels A-D demonstrated histological staining and cell morphology in different regions of the regenerating tissue and surrounding articular cartilage. Abbreviations: P for PCL strands. Scale bars: A-D = 1 mm; A′-D‴ = 200 μm.

seen at both timepoints, but appeared to increase from one- to three-months post-implantation (figures 5(A) and (E). Col II was deposited at deeper regions of hydrogel-treated defects at the one-month timepoint, and the margins of regenerated tissues were easily recognized (figure 5(A)). By three months, Col II deposition was detected from deep to superficial regions of the regenerated tissue, and the margins were less noticeable (figure 5(E)). Hybrid-treated defects showed very faint Col II immunostaining in regenerating tissues at one-month post-implantation (figure 5(B)), but by three months, Col II deposition seemed to increase compared to the one-month timepoint (figure 5(G)). Interestingly, hybrid-treated defects with fewer visible PCL strands showed higher Col II deposition. The amount of Col II deposited in hybrid-treated defects at three months appeared to be less than that deposited in hydrogel-treated defects, with only deep regions showing Col II immunoreactivity. Integration with adjacent cartilage in the margins of hybrid-treated defects also seemed to be less than in hydrogel-treated defects.

Similarities between GAG and Col II depositions further confirmed the cartilaginous nature of regenerated tissues in both hydrogel-treated and hybrid-treated defects. Compared to Safranin O staining (figure 3), Col II immunofluorescence occurred in similar regions of both hydrogel-treated and hybrid-treated defects (figure 5), with more Col II seen at marginal regions of 1 month defects and central regions of 3 month defects. Taken together, all these data suggested the cartilage formation at both treated defects though what kind of cartilage (either hyaline cartilage or fibrocartilage) remained unclear. To make this clear, Col I immunostaining was also employed because Col I is a marker of fibrocartilage [58]. In particular, overlaying images of Col I and Col II immunostaining allowed localization of where Col I and Col II were co-deposited (see supplemental figure 3). At the hydrogel-treated defects at one-month post-implantation, Col I immunostaining was only seen in superficial regions of regenerating tissues, resembling the superficial zone of articular cartilage (figure (B)). Comparing Col I regions to Col II, Col II-positive, Col I-negative regions seen deeper within regenerating tissue suggested hyaline cartilage formation at these locations (figures 5(A) and (B)). In the hybrid-treated defects at one-month post-implantation, Col I immunostaining was also abundant at superficial regions of regenerating tissues, but significant Col I was detected between PCL strands in slightly deeper regions (figure 5(D)). Since

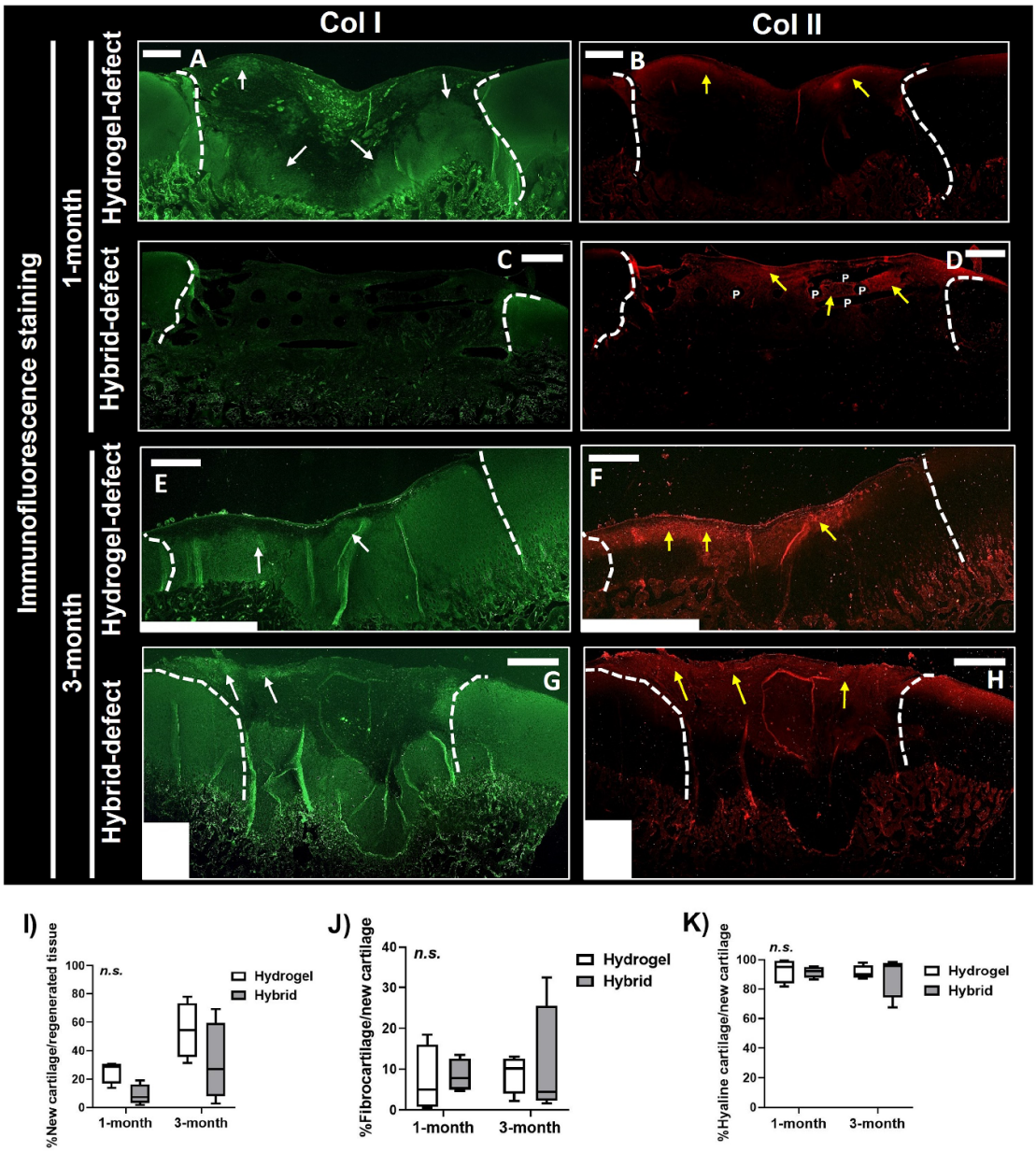

Figure 5. Immunostaining showed that cartilage formation increased over time in both treated defects, but Col I immunostaining suggested that fibrous tissue and fibrocartilage were common. (A), (B) Col II immunostaining was moderate in deep regions of regenerating tissues (dashed lines) in hydrogel-treated defects at one-month post-implantation (white arrows), with weak staining for Col I at superficial regions (yellow arrows). (C), (D) Hybrid-treated defects had little to no Col II immunostaining in regenerating tissues (dashed lines), with some Col I immunostaining in superficial regions. (E), (F) Col II deposition (white arrows) was enhanced throughout regenerating tissues (dashed lines) of hydrogel-treated defects by three-months post-implantation, with higher Col I deposition (yellow arrows) at superficial regions. (G), (H) Hybrid-treated defects at three months showed Col II deposition (white arrows) mostly in deeper regions of regenerating tissues (to the right of the dashed line), and Col I was deposited (yellow arrows) mostly at superficial regions of these defects. Immunostaining quantitation showed that cartilage regeneration trended higher over time, and fibrocartilage levels were relatively low. (I) New cartilage regeneration trended higher in hydrogel-treated defects than the hybrid-treated defects at both time points. (J) Fibrocartilage formation showed an increasing and decreasing trend for hydrogel-treated defects and hybrid-treated defects, respectively. (K) Hyaline cartilage regeneration accounted for most of the formed cartilage in both types of defects at both time points. n = 4 for these analyses. Abbreviations: P = PCL strand. Scale bars: A-H = 1 mm.

these regions between PCL strands had little to no Col II detected, Col I immunostaining likely reflected fibrous tissue. By three-months post-implantation, Col I deposition had increased at superficial regions of hydrogel-treated defects, but remained at similar levels in hybrid-treated defects (figures 5(F) and (H)). In hydrogel-treated defects at three-months post-implantation, overlapping Col I and Col II deposition at superficial regions of the regenerating tissue resembled the superficial zone of healthy articular cartilage (figures 5(E) and (F)). Covering this superficial region in hydrogel-treated defects, however, was a thin layer with low Col I and no Col II deposition that did not exist in native cartilage. In hybrid-treated defects at three-months post-implantation, Col I deposition was relatively high in

superficial regions of the regenerating tissue, but deep to this region was a large region with little Col I and no Col II deposition, likely representing fibrous tissue (figures 5(G) and (H)).

In order to more accurately and objectively compare total cartilage (Col II-positive area), fibrocartilage (Col I-positive/Col II-positive area), and hyaline cartilage (Col I-negative/Col II-positive area) in regenerating tissues, immunofluorescence images were quantitated. Total cartilage regeneration (i.e. Col II-positive area/regenerated tissue area) tended to be higher in hydrogel-treated defects compared to hybrid-treated defects at both timepoints (figure 5(I)). At one-month post-implantation, 23.8 ± 5.1% cartilage regeneration was observed in hydrogel-treated defects, which tended to increase to 52.7 ± 13.6% by three-months (figure 5(I)). Over time, cartilage regeneration also tended to increase within hybrid-treated defects from 5.6 ± 1.8% to 32.0 ± 19.6% (figure 5(I)), although no quantitation of cartilage regeneration was statistically significant between timepoints for a given group or between groups for a given timepoint.

Quantitating how much of the Col II-positive tissue was also Col I-positive showed that formation of fibrocartilage was relatively low at both timepoints and hyaline cartilage was relatively high. At one-month post-implantation, Col I-positive areas within Col II-positive areas trended higher in hybrid-treated defects (6.8 ± 1.5%) than hydrogel-treated defects (3.5 ± 2.6%) (figure 5(J)). By three-months, however, fibrocartilage regeneration trended higher in hydrogel-treated defects (11.1 ± 1.1%) than hybrid-treated defects (3.5 ± 1.0%) (figure 5(J)). Similar quantitation of hyaline cartilage regeneration showed an inverse trend compared to fibrocartilage formation, as these measurements represented complementary percentages as they were defined. As such, for hydrogel-treated defects at one- and three-months post-implantation, the percentage of hyaline cartilage within total regenerating cartilage was 96.5 ± 2.6% and 88.9 ± 1.1%, respectively (figure 5(K)). This quantitation was 93.2 ± 1.5% and 96.5 ± 1.0% in hybrid-treated defects, respectively (figure 5(K)). These analyses showed that most of the formed cartilage seemed to be hyaline cartilage, although no quantitation of fibrocartilage or hyaline cartilage was statistically significant between timepoints for a given group or between groups for a given timepoint.

3.4. Synchrotron inline-PCI-CT revealed high-resolution details at the treated defects, including a correlation between pixel intensities of virtual slices and Safranin O-stained sections

To provide a non-invasive view of various tissues and biomaterials within and surrounding femoral condyle defects, excised samples were imaged using synchrotron radiation-based inline phase contrast with computed tomography (inline-PCI-CT) and 3D reconstructed. Virtual slices from these reconstructions (inline-PCI-CT slices) clearly depicted regenerating tissue in the defects at high resolution, PCL strands for hybrid-treated defects, surrounding native cartilage, and subchondral bone (figures 6(A) and (B)). Due to high absorption properties, mineralized subchondral bone had the brightest pixels, but surrounding unmineralized articular cartilage and regenerating tissues were also evident, due the edge enhancement from phase contrast image processing [59]. In hybrid-treated defects, PCL strands were obvious in inline-PCI-CT slices (figure 6(B)). Therefore, the high resolution and increased contrast of inline-PCI-CT enabled evaluation of many discrete features of value for CTE.

Comparatively, inline-PCI-CT slices were examined alongside corresponding tissue sections stained with Safranin O to illustrate its ability to provide biologically-meaningful information non-invasively. Overall tissue morphology confirmed that the specific virtual slices of hydrogel-treated defect and hybrid-treated defect samples matched well with the selected histological tissue sections (figures 6(A)–(D)). As with Safranin O-stained sections, inline-PCI-CT slices of both types of defect visualized the margins between defect regions and surrounding host tissues (figures 6(A)–(D)). Visualization of biomaterials was very different between inline-PCI-CT slices and Safranin O-stained tissue sections. Inline-PCI-CT slices showed individual PCL strands at high contrast within hybrid-treated defects, even if PCL strands were extremely close to one another (figures 6(B) and (B′)). In histological sections, however, close PCL strands were not easily discernible (figures 6(D) and (D′)). Integrity of the tissues and cellular resolution (under the specific synchrotron imaging settings) also varied. Wrinkles and tears were often observed in Safranin O-stained sections, whereas inline-PCI-CT slices were free of such artifacts (figures 6(A)–(D)). Individual cells were discernible in Safranin O-stained section, but not in the inline-PCI-CT virtual slices (e.g. figures 6(A′) and (C′)).

Unexpected variations in pixel intensities were observed in different regions of cartilage in inline-PCI-CT slices, and these differences seemed to correlate with pixel intensities in Safranin O-stained tissue sections. Higher gray-value pixel intensities in inline-PCI-CT slices were observed at deeper regions of both the regenerating and surrounding native cartilage of hydrogel-treated defects at one-month post-implantation, while more superficial regions had lower pixel intensities (figure 6(A)). Similar trends were observed in native cartilage of hybrid-treated defects, but pixel intensities were generally low in the regenerating tissues (figure (B)). Similar intensity changes were observed in Safranin O staining of sulfated GAGs in tissue sections that corresponded to the virtual inline-PCI-CT slices. In both

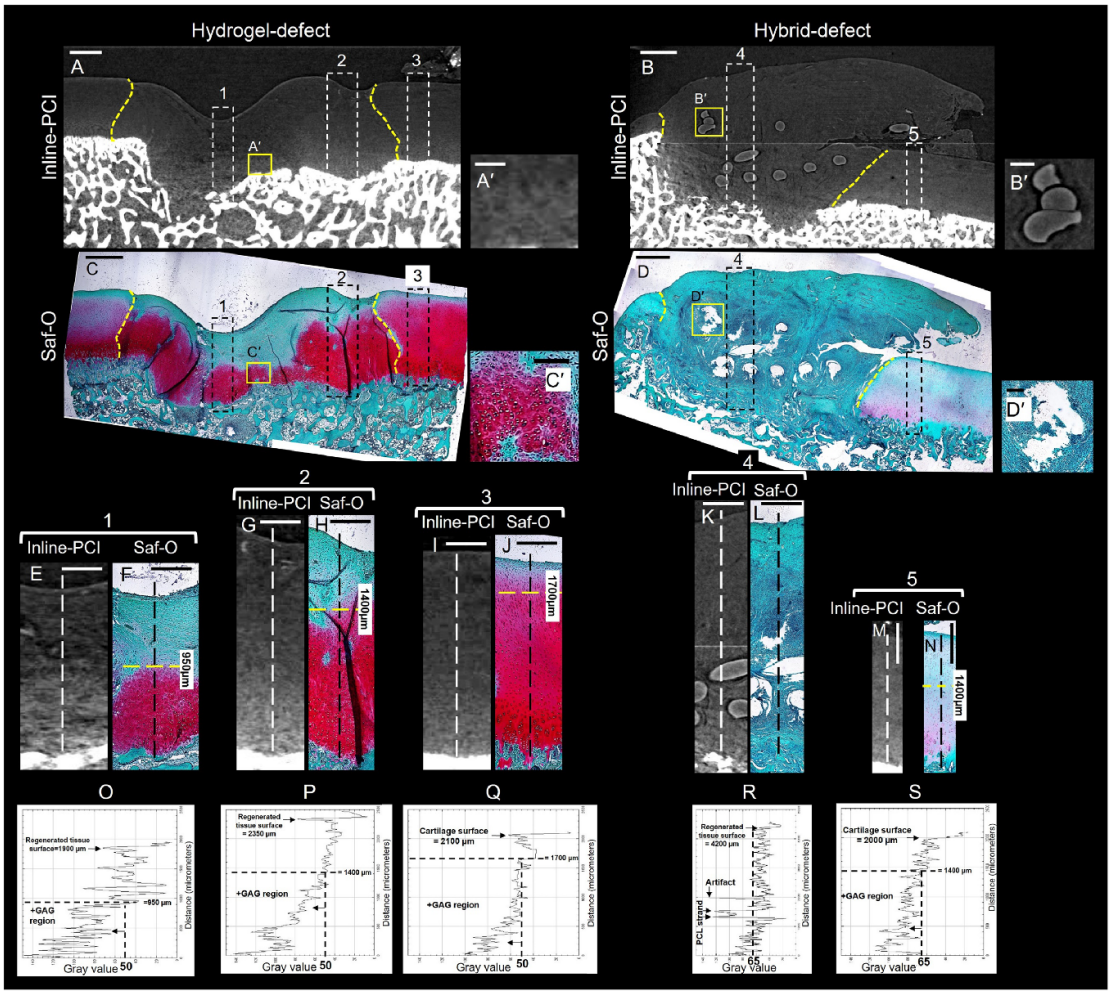

Figure 6. Synchrotron inline-PCI-CT revealed high-resolution details of defects, including a correlation between pixel intensities of virtual slices and Safranin O-stained sections. (A)–(D) Both hydrogel-treated defect and hybrid-treated defect inline-PCI-CT slices showed high-resolution details of regenerating (yellow dashed lines) and surrounding native tissues and biomaterials. Also, their gray-value pixel intensities had good correlation with red pixel intensities in corresponding Safranin O sections of similar regions. (B)–(B′) Inline-PCI-CT slices were advantageous in discerning close PCL strands, and (C)–(C′) Safranin O-stained sections were able to visualize resident cells (regions A′–D′ indicated on panels (A)–(D)). (E)–(N) Variations in gray-value pixel intensities of inline-PCI-CT slices through the depth of both regenerating and native cartilage appeared to correlate with Safranin O staining levels (regions 1-5 in panels E-N are illustrated on panels (A)–(D)). (O)–(S) Gray-value histograms (vertical dashed lines in panels E-N) through regenerating and native cartilage confirmed this correlation. Scale bars: A-D = 1000 μm; A′-D′ = 200 μm; E-N = 500 μm.

hydrogel-treated defects and hybrid-treated defects, Safranin O-stained tissue sections appeared to have higher and lower red pixel intensity in the exact regions where inline-PCI-CT slices showed higher and lower gray-value pixel intensities, respectively (figures 6(E)–(N)).

Quantitative analyses of representative histogram traces of inline-PCI-CT slices along the depth of either regenerating tissue or surrounding native cartilage supported a correlation between the gray-value pixel intensities and sulfated GAG staining by Safranin O. According to the gray-value histograms (vertical dashed lines on figures 6(E)–(N)), most pixels that had higher Safranin O staining (see horizontal dashed lines on figures 6(F), (H), (J) and (N)) generally were above a certain 'boundary' gray value (figures 6(O)–(S)). The absolute boundary gray value could vary between samples, but gray values generally dropped below this boundary at regions showing little Safranin O staining (figure (E)–(S)). The correlation between inline-PCI-CT slices and Safranin O staining was not only seen in native cartilage, but also in regenerating tissue (figures 6(O)–(S)). For example, higher Safranin O staining was found at various ranges above the subchondral bone surface of a hydrogel-treated defect (e.g. up to 1700 μm, 1400 μm, and 950 μm for surrounding native cartilage, marginal regenerating tissue, and central regenerating tissue, respectively) (dashed yellow lines on figures 6(F), (H) and (J)). A corresponding inline-PCI-CT slice had boundary gray values that correlated very well with the higher Safranin O-stained sulfated GAGs; most pixels were over a boundary gray value of 50 in those same ranges above the surface

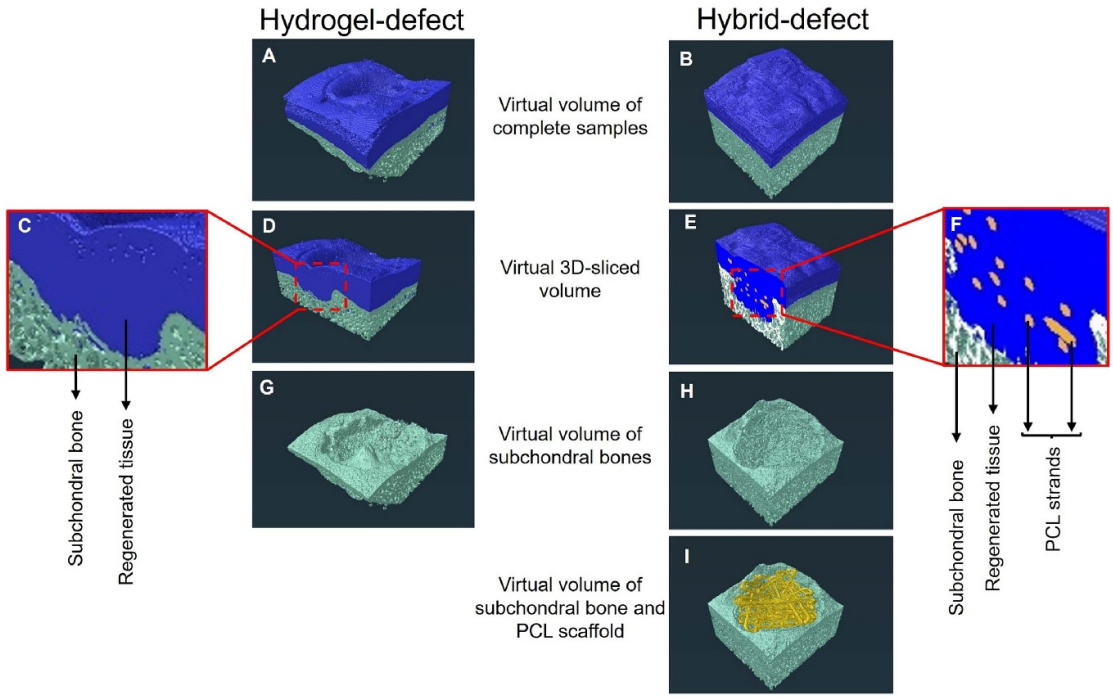

Figure 7. 3D volume rendering of segmented inline-PCI-CT datasets allowed non-invasive evaluation of *in vivo*-implanted, 3D-bioprinted cartilage tissue engineering constructs. 3D volume rendering of hydrogel-treated defects (A), (C), (D), (G) and hybrid-treated defects (B), (E), (F), (H), (I) visualized 3D morphology of different components, such as subchondral bone, regenerating and surrounding native tissues, and PCL strands, either individually or collectively in 3D. The samples could be 3D-cut at any region to look at morphological features of defects. Hybrid-treated defects were deeper into the subchondral bone compared to hydrogel-treated defects.

of the subchondral bone (figures 6(O)–(Q)). Hybrid-treated defects also showed large gray-value peaks at the edges of PCL strands (figure 6(R)).

3.5. Segmentation of inline-PCI-CT data non-invasively highlighted 3D relationships among various components, including PCL strands and loss of subchondral bone in hybrid-treated defects

To better understand 3D morphological relationships between various tissues and biomaterials within and surrounding the femoral condyle defects one-month post-implantation, inline-PCI-CT slices underwent segmentation of subchondral bone, newly regenerating and surrounding native tissues, and PCL strands (figure 7). Regenerating tissues over the defects were not as smooth as the adjacent native cartilage, presenting depressed surfaces on top of both hydrogel-treated defects and hybrid-treated defects, although this was more common in hydrogel-treated defects (figures 7(A) and (B)). After segmentation, spatial relationships between subchondral bone, regenerating and native tissues, and PCL strands could be easily discerned on sliced views through the 3D-rendered volume (figures 7(C)–(F)). In both groups, the subchondral bone surface was unexpectedly found to be depressed away from the articular surface below the defect (figures 7(C)–(H)), even though the initial surgical defect was only drilled down to the surface of subchondral bone. Supporting the idea that the 3D-bioprinted constructs played a role in this feature, depressions into subchondral bone were more common and obvious in hybrid-treated defects. At one-month post-implantation, PCL strands maintained their printed orientation in some of the hybrid-treated defects samples (figure 7(I)). By three-months post-implantation, inline-PCI-CT demonstrated that most hybrid-treated defects had missing, disoriented, and damaged strands that were displaced into deeper subchondral regions, confirming the histology findings (data not shown). In summary, synchrotron-based inline-PCI-CT proved to be an effective non-invasive alternative to traditional methods for evaluating features of the *in vivo*-implanted 3D-bioprinted constructs.

4. Discussion

A major goal of CTE is to treat defects in articular cartilage by producing cartilaginous molecules including GAGs and Col II (both are the indications of hyaline cartilage) [16, 60]. However, there has been limited exploration of simultaneous examinations of Col I (a fibrocartilaginous molecule) and Col II *in vivo*, despite the fact that previous studies hinted the potential formation of fibrocartilage within the hydrogels subjected to mechanical forces both *in vitro* and *in vivo* [21–23]. In this paper, we present a comparative study

on the formation of hyaline cartilage versus fibrocartilage in a large animal model of pigs, employing two types of constructs i.e. hydrogel and hybrid constructs. We also explored the potential use of an inline-PCI-CT technique for monitoring cartilage regeneration within large animal models.

Over time, gross observations of either type of treated defect showed increased regenerating tissue formation and integration with surrounding native cartilage. According to the Wayne *et al* scoring system [49], gross anatomical measures of femoral condyle defects treated with hydrogel constructs (hydrogel-treated defects) were slightly higher than those treated with hybrid constructs at both one- and three-months post-implantation, but these differences were not statistically significant. In fact, many of the quantitative measures of cartilage regeneration in this study were not statistically significant, despite methodological approaches undertaken, like averaging measures across many regions of each histologically-prepared sample. The likely major causes of this lack of statistical power are that *in vivo* experiments are generally complicated by numerous factors outside of control, and large animal studies are very expensive, limiting the overall sample size possible under a given budget. In any case, macroscopic observations suggested that white translucent cartilage-like tissues progressively covered the defects over time.

Multiple techniques, including Safranin O, Trichrome, and Col II immunofluorescent staining, demonstrated an increase in cartilage formation over time in both hydrogel-treated and hybrid-treated defects. Specifically, these stains showed deposition of sulfated GAGs and Col II, two of major components of cartilage ECM [12]. The organization and shape of cells also resembled hyaline cartilage at one-month post-implantation in hydrogel-treated defects and at three-months for both treated defects. While the observed cartilage formation seemed to increase over time, no samples had completely filled the defects with regenerated cartilage by three-months, suggesting that for large animal models with large defects (8 mm in this study), timepoints longer than three months would be required for complete cartilage regeneration.

Hydrogel constructs seemed to be more effective in cartilage regeneration than hybrid constructs at both timepoints. At one-month post-implantation, hydrogel-treated defects already appeared to have high amounts of sulfated GAG staining and Col II immunofluorescence, while almost no staining was observed in hybrid-treated defects. However, hybrid constructs had both PCL and alginate strands, while hydrogel constructs were comprised of only cell-impregnated alginate strands. According to these differences in fabrication methods, hybrid constructs used in the study contained fewer cells, compared to the hydrogel-only constructs, which could have led to lower performance. Similar to results from this study, a previous study reported that 3D-bioprinted collagen/PCL hybrid constructs had little or no cartilage formation *in vivo* over 8 weeks, while 3D-bioprinted collagen hydrogels supported cartilage regeneration [61]. These authors related failure of the hybrid constructs to excessive mechanical strength of collagen/PCL hybrid structure [61], and our data expand upon future problems to be solved in the hybrid approach. Indeed, despite enhanced GAG and Col II deposition in hybrid-treated defects by three-months post-implantation, this cartilage formation actually occurred at regions where fewer PCL strands were present.

What might be the influence of PCL strands on cartilage regeneration? Several *in vivo* studies that implanted PCL constructs into articular cartilage showed similar results as reported here, with either fibrous formation or little to no cartilage regeneration around the PCL structures [61–63]. In our study, PCL strands seemed to be in the correct structure and location within the defect at one-month post-implantation, but fewer strands were seen at three months, which agrees with a similar study reporting about 80% PCL volume loss from osteochondral defects in an equine model [62]. The loss of PCL strands is unlikely due to degradation, since the PCL degradation period is up to 3–4 years [64], and more likely resulted from mechanical forces in the joints causing damage to the PCL structure, either pushing it down into the subchondral bone or causing some of the damaged and broken PCL strands to be lost from the defect region. Indeed, hybrid-treated defects seemed to have greater degradation of subchondral bone than hydrogel-treated defects, aligning with previous suggestions [62]. The collapse of adjacent articular cartilage into the defects also probably contributed to subchondral bone degradation by causing excessive forces inward. As for the influence of PCL on cartilage regeneration, this study, and potentially previous studies, are inconclusive, as the PCL seemed to be displaced far from the surface of the regenerating defect by three-months post-implantation. Notably, earlier studies on smaller animals like rabbits and minipigs revealed similar outcomes, where PCL structures were displaced to lower regions of the subchondral bone, leading to severe bone lysis [63]. However, in those cases, the dislocated strands retained their configuration and were not extensively damaged. In contrast, our results reveal that not only did the PCL structure contribute to subchondral bone degradation, but the PCL strands were also damaged by three-months post-implantation, losing their printed structure. The quantity of PCL strands within the defect regions appeared visually diminished three-months post-implantation. This potential structural loss may be associated with the damage of the PCL strands and their subsequent loss from the defect site. This emphasizes the intricate mechanical forces inherent in larger animals and underscores the

importance of conducting *in vivo* cartilage research in such contexts to observe the effects of higher mechanical forces, aligning with those found in human joints. Thus, it is urged further modifications are necessary for 3D bioprinted hybrid constructs to maintain PCL strands in place, enabling them to withstand applied mechanical forces in joints for the duration required for new hyaline cartilage to be generated and replace the naturally degraded PCL. Of note, alginate strands were not visible in either hydrogel-treated defects or hybrid-treated defects, with two possible explanations: (1) the strands degraded in response to the *in vivo* conditions of the joints; or (2) they remained at the defect and blended so intimately into the surrounding tissues that our histological and imaging protocols could not distinguish them.

In this study, a critical focus was placed on immunofluorescence staining for Col I and Col II deposition to assess whether hyaline cartilage or fibrocartilage was formed at the treated defects. This also allowed for assessing whether hybrid constructs could mitigate fibrocartilage formation, as reported previously [21–23]. *In vitro*, hydrogel constructs under cyclic compression loading tended to produce more hyaline-like cartilage ECM compared to PCL-reinforced hydrogel constructs [55] However, it is important to note that these *in vitro* experiments were conducted under unconfined compression conditions, which may differ from the confined conditions experienced *in vivo*. This limitation highlights that the findings observed in the *in vitro* environment may not be replicated in the complex *in vivo* setting. In the current study, hydrogel-treated defects exhibited a similar amount and location of Col I and Col II deposition as seen in the surrounding native articular cartilage, predominantly at the superficial regions of the defects, at both timepoints. At one-month post-implantation, Col I deposition in hybrid-treated defects was also in superficial regions, but appeared somewhat increased a bit deeper after three months. However, these regions did not have evidence of Col II deposition, indicating simple fibrous or undifferentiated tissue, rather than fibrocartilage. Quantitatively, our study demonstrated that fibrocartilage levels tended to decrease in hybrid-treated defects three months post-implantation compared to hydrogel-treated defects, where fibrocartilage formation increased over time. This supports our hypothesis that excessive mechanical forces exerted on cells within engineered hydrogel constructs promote fibrocartilage formation at knee joints. Also, 3D-bioprinted hybrid constructs, based on the force-shielding mechanism, allowed reducing the forces on cells within alginate hydrogel strands and thus diminishing the Col I and fibrocartilage production. It is noted that the observed loss of PCL strands in the treated defects may diminish the PLC role in force shielding. Meanwhile it is worthwhile to note that at the treated defects, the regenerated cartilage along with its the integration of the surrounding tissues imparts the construct strength, thus compensating for the loss of PCL strands.

Some mechanical features, such as the fast stress relaxation seen in alginate hydrogels, can increase ECM production by chondrocytes [65], which might explain why hydrogel-treated defects appeared to have more regenerating cartilage than hybrid-treated defects. Slower relaxing environments restrict cell volume expansion, and increase cell death and catabolic gene expression through activation of IL-1β signaling [66]. Furthermore, increased stiffness of fabricated constructs results in minimal stress relaxation, which inhibits the production of GAGs and collagens, cartilage matrix distribution, and chondrocyte proliferation [66]. In the present study, regenerative cells within or beneath the PCL structure were in a stiffer environment than the cells in hydrogel-treated defects while being subjected to high biomechanical forces of the joint. These factors could potentially contribute to the lower production of GAGs and collagen observed in hybrid-treated defects. However, detailed investigations were not conducted in this regard. Future research into cellular mechanisms of mechanotransduction would help in understanding how cells in different 3D-bioprinted constructs respond to their biomechanical environment.

What was the cellular source of regenerating tissues? Chondrogenic ATDC5 cells were impregnated into both constructs in this study, but no evidence of an immune response was observed at any point after implantation of these mouse cells into pig articular cartilage. Two explanations are likely. First, the alginate surrounding these cells shielded them from immune detection, at least at early timepoints. Second, the synovial joint capsule has generally low immunosurveillance, limiting an immune response [67]. In addition to the possibility that ATDC5 cells contributed to regenerating cartilage as per this study, local stem cells might have been recruited in a similar fashion to the microfracture surgery [7, 68], given that the defects were surgically created down to subchondral bone of the pig femoral condyles. Being consistent with this idea, early regenerating cartilage was often observed to apparently extend from native surrounding cartilage in deeper regions close to the subchondral bone. It may be interesting for future experiments to help discover the cellular source of regenerating cartilage at these defects. For this, scaffolds without cells may be implanted alongside cell-impregnated constructs for comparison. Also, the molecular markers of the cellular origin of regenerating tissues may be assayed, e.g., the mouse-specific HLA antibodies or even transgenic or otherwise labelled cells could be employed for future studies. Additionally, it is noted that the cell lines used in this study have a relatively higher proliferation rate compared to primary chondrocytes or MSCs, which are commonly used in clinical trials with slower

expansion and tissue regeneration. Since primary cells have a more complex phenotype, which might influence differentiation pathways and the quality of the regenerated tissue, future studies are urged to discover the influence of these factors. Meanwhile, it would be interesting to develop strategies to enhance the primary cell-expansion rate to achieve optimal outcomes.

In efforts to increase non-invasive visualization of regenerating tissues in CTE, we explored the potential of a novel synchrotron radiation-based method, inline-PCI-CT [30]. Traditional methods limit spatial understanding and require many animals for longitudinal studies, raising concerns about cost and animal use. Furthermore, transitioning to human studies demands non-invasive imaging for examining tissue regeneration at intermediate stages. Our findings from inline-PCI-CT demonstrated that this state-of-the-art tool provides user-defined 2D and 3D views of regions of interest, in contrast to traditional invasive methods, such as histology and immunofluorescence, which are limited to 2D views [32]. With x-ray absorption and phase contrast edge enhancement, inline-PCI-CT visualized at high resolution implanted PCL strands, regenerating tissue within the defects, and surrounding bone and cartilage. In comparison to histology images, inline-PCI-CT images were free from wrinkles and tears and allowed direct visualization of PCL strands instead of inferring them from spaces after xylene extraction. While cartilaginous features at the cellular level have been observed by inline-PCI-CT and were validated by standard histology [69], the current study is the first to demonstrate a clear correlation between gray-value pixels of inline-PCI-CT virtual slices and sulfated GAG deposition, verified by Safranin O histology. Higher gray-value pixel intensities within regions containing more sulfated GAGs might result from higher mass densities, since inline-PCI-CT imaging is highly responsive to mass density changes [70]. Since GAG sulfation dictates the chemical and biological functions of cartilage matrix [71], such imaging correlations might allow non-invasive assessment of cartilage function. A further advantage of inline-PCI-CT scanning was the ability to examine overall 3D morphology of the regenerated tissue, as well as its 3D relationships with surrounding tissues. These features facilitated the straightforward identification of subchondral bone depressions within the defects, further confirming the importance of conducting studies on the knees of large animals for the purpose of cartilage regeneration. These alterations were previously demonstrated through our histology stainings; however, studying them using traditional histological techniques would have required laboriously sectioning the entire sample, imaging it, and digitally reconstructing it to obtain views of various regions. This process is both time-consuming and effort-intensive, while inline-PCI-CT images makes it more efficient and faster to observe different locations in both 2D and 3D.The exact radiation dose used in our study is still unsuitable for imaging living animals, although recent studies have begun to develop appropriate protocols that maximize imaging resolution while minimizing effective dose [72, 73]. Overall, our imaging findings demonstrated that inline-PCI-CT can provide great insight for investigators who are considering the *in vivo* characterization of tissue engineered constructs for cartilage regeneration.

5. Conclusions

Both hyaline cartilage and fibrocartilage formation are concerned in cartilage tissue engineering, which, however, have not been investigated simultaneously, as well as in large animal models or those similar to humans. This paper presents our comparative study on the hyaline cartilage and fibrocartilage formation in a pig model by employing 3D-bioprinted hydrogel and hybrid constructs.

Our results by means of multiple assays or techniques showed that cartilage formation increased at both hydrogel- and hybrid-treated defect sites over the time period of three months as we examined, while the overall cartilage regeneration was more promising at the hydrogel-treated defects as compared to the hybrid-treated defects. The presence of GAGs and Col II, essential components of cartilage ECM, was observed at one-month post-implantation in hydrogel-treated defects and at three months for both treated defect sites. According to GAGs and Col II depositions, hydrogel construct showed higher levels of cartilage formation at both one and three months after implantation as compared to the hybrid constructs. Our results also showed that fibrocartilage tended to decrease in hybrid-treated defects at three-months post-implantation compared to hydrogel-treated defects, where the formation of fibrocartilage increased over the examination time. This finding is in support of that the excessive mechanical forces exerted on the cells within engineered hydrogel constructs do promote the fibrocartilage formation at the knee joints, as we hypothesized. Concurrently, our imaging results demonstrated that the gray-value pixels from inline-PCI-CT images correlated with the amount of GAG staining by Safranin O, suggesting that inline-PCI-CT be promising as an alternative to histological methods in characterizing cartilage regeneration. This would represent a significant advance toward the non-invasive assessment of cartilage formation regeneration, which is essential to human patients in the future. Interestingly, our imaging data on 3D volume-rendered views of inline-PCI-CT also revealed the information on the

PCL strands or structures at the defect sites, showing that over the examination time period, the PCL strands are changed in their orientation, as well as allocations from the region defect into subchondral bone, which may cause subchondral bone degradation.

Taken together, this study contributes to the investigation of hyaline and fibrocartilage formation *in vivo* using 3D-bioprinted constructs and examines cartilage regeneration in pig knee joints, which replicate human knee biomechanics. Additionally, it pioneers the non-invasive assessment of cartilage regeneration in large animal models and potentially in humans using inline-PCI-CT.

Data availability statement

All data that support the findings of this study are included within the article (and any supplementary files).

Author contributions

Conceptualization was done by H A S, X C, A H, and B F E; B F E and X C provided project supervision, while A H coordinated supervised surgeries performed by G D S R and W D; H A S, G D S R, and G R wrote ethical SOPs and protocols; G R, S B, and A C monitored surgeries and anesthesia; T C C assisted surgeries and sample excision; H A S 3D-bioprinted the constructs, scanned the samples at CLS, and performed all analyses, while also writing the original draft; Review/editing was done by H A S, X C, A H, and B F E, and all authors have read and agreed to the published version of the manuscript.

Funding

This study was supported by the University of Saskatchewan Devolved Graduate Scholarship to H A S, Natural Sciences and Engineering Research Council of Canada (NSERC) Discovery Grant (RGPIN 06396-2019) to X C, and a University of Saskatchewan CoMBRIDGE grant to B F E.

Conflict of interest

The authors declare no conflict of interest.

ORCID iDs

Hamed Alizadeh Sardroud https://orcid.org/0009-0002-5534-7768
Ali Honaramooz https://orcid.org/0000-0002-3194-9468
Xiongbiao Chen https://orcid.org/0000-0002-4716-549X

References

[1] Buckwalter J A and Lane N E 1996 Aging, sports, and osteoarthritis *Sports Med. Arthroscopy Rev.* **4** 276–87
[2] Mankin H J 1982 The response of articular cartilage to mechanical injury *JBJS* **64** 460–6
[3] Hunziker E B 2002 Articular cartilage repair: basic science and clinical progress. A review of the current status and prospects *Osteoarthritis Cartilage* **10** 432–63
[4] Neuprez A, Neuprez A H, Kaux J-F, Kurth W, Daniel C, Thirion T, Huskin J-P, Gillet P, Bruyère O and Reginster J-Y 2020 Total joint replacement improves pain, functional quality of life, and health utilities in patients with late-stage knee and hip osteoarthritis for up to 5 years *Clin. Rheumatol.* **39** 861–71
[5] Brittberg M, Lindahl A, Nilsson A, Ohlsson C, Isaksson O and Peterson L 1994 Treatment of full-thickness cartilage defects in the human knee with cultured autologous chondrocytes *Neq Engl. J. Med.* **331** 889–95
[6] Orozco L, Munar A, Soler R, Alberca M, Soler F, Huguet M, Sentís J, Sánchez A and García-Sancho J 2013 Treatment of knee osteoarthritis with autologous mesenchymal stem cells: a pilot study *Transplantation* **95** 1535–41
[7] Mithoefer K, McAdams T, Williams R J, Kreuz P C and Mandelbaum B R 2009 Clinical efficacy of the microfracture technique for articular cartilage repair in the knee: an evidence-based systematic analysis *Am. J. Sports Med.* **37** 2053–63
[8] Moseley J B, O'malley K, Petersen N J, Menke T J, Brody B A, Kuykendall D H, Hollingsworth J C, Ashton C M and Wray N P 2002 A controlled trial of arthroscopic surgery for osteoarthritis of the knee *New Engl. J. Med.* **347** 81–88
[9] O'Driscoll S W, Keeley F and Salter R 1986 The chondrogenic potential of free autogenous periosteal grafts for biological resurfacing of major full-thickness defects in joint surfaces under the influence of continuous passive motion. An experimental investigation in the rabbit *J. Bone Hoint Surg. Am.* **68** 1017–35
[10] Bedi A, Feeley B T and Williams R J III 2010 Management of articular cartilage defects of the knee *JBJS* **92** 994–1009
[11] Frisbie D D, Oxford J T, Southwood L, Trotter G W, Rodkey W G, Steadman J R, Goodnight J L and McIlwraith C W 2003 Early events in cartilage repair after subchondral bone microfracture *Clin. Orthop. Relat. Res.* **407** 215–27
[12] Becerra J, Andrades J A, Guerado E, Zamora-Navas P, López-Puertas J M and Reddi A H 2010 Articular cartilage: structure and regeneration *Tissue Eng.* B **16** 617–27
[13] Alizadeh Sardroud H, Wanlin T, Chen X and Eames B F 2022 Cartilage tissue engineering approaches need to assess fibrocartilage when hydrogel constructs are mechanically loaded *Front. Bioeng. Biotechnol.* **9** 1388
[14] Balakrishnan B and Banerjee R 2011 Biopolymer-based hydrogels for cartilage tissue engineering *Chem. Rev.* **111** 4453–74
[15] You F, Wu X, Zhu N, Lei M, Eames B F and Chen X 2016 3D printing of porous cell-laden hydrogel constructs for potential applications in cartilage tissue engineering *ACS Biomater. Sci. Eng.* **2** 1200–10
[16] Lan X *et al* 2021 Bioprinting of human nasoseptal chondrocytes-laden collagen hydrogel for cartilage tissue engineering *FASEB J.* **35** e21191
[17] Grodzinsky A J, Levenston M E, Jin M and Frank E H 2000 Cartilage tissue remodeling in response to mechanical forces *Annu. Rev. Biomed. Eng.* **2** 691–713
[18] Van Susante J L C, Buma P, Schuman L, Homminga G N, van den Berg W B and Veth R P H 1999 Resurfacing potential of heterologous chondrocytes suspended in fibrin glue in large full-thickness defects of femoral articular cartilage: an experimental study in the goat *Biomaterials* **20** 1167–75

[19] Kim K, Lam J, Lu S, Spicer P P, Lueckgen A, Tabata Y, Wong M E, Jansen J A, Mikos A G and Kasper F K 2013 Osteochondral tissue regeneration using a bilayered composite hydrogel with modulating dual growth factor release kinetics in a rabbit model *J. Control. Release* **168** 166–78
[20] Holland T A, Bodde E W H, Baggett L S, Tabata Y, Mikos A G and Jansen J A 2005 Osteochondral repair in the rabbit model utilizing bilayered, degradable oligo (poly (ethylene glycol) fumarate) hydrogel scaffolds *J. Biomed. Mater. Res.* A **75** 156–67
[21] Schagemann J C, Erggelet C, Chung H-W, Lahm A, Kurz H and Mrosek E H 2009 Cell-laden and cell-free biopolymer hydrogel for the treatment of osteochondral defects in a sheep model *Tissue Eng.* A **15** 75–82
[22] Marquass B *et al* 2011 Matrix-associated implantation of predifferentiated mesenchymal stem cells versus articular chondrocytes: in vivo results of cartilage repair after 1 year *Am. J. Sports Med.* **39** 1401–12
[23] Lee C R, Grad S, Gorna K, Gogolewski S, Goessl A and Alini M 2005 Fibrin–polyurethane composites for articular cartilage tissue engineering: a preliminary analysis *Tissue Eng.* **11** 1562–73
[24] Kundu J, Shim J-H, Jang J, Kim S-W and Cho D-W 2015 An additive manufacturing-based PCL–alginate–chondrocyte bioprinted scaffold for cartilage tissue engineering *J. Tissue Eng. Regen. Med.* **9** 1286–97
[25] Izadifar Z, Chang T, Kulyk W, Chen X and Eames B F 2016 Analyzing biological performance of 3D-printed, cell-impregnated hybrid constructs for cartilage tissue engineering *Tissue Eng.* C **22** 173–88
[26] Olubamiji A D, Izadifar Z, Zhu N, Chang T, Chen X and Eames B F 2016 Using synchrotron radiation inline phase-contrast imaging computed tomography to visualize three-dimensional printed hybrid constructs for cartilage tissue engineering *J. Synchrotron Radiat.* **23** 802–12
[27] Izadifar Z, Chapman L D and Chen X 2014 Computed tomography diffraction-enhanced imaging for in situ visualization of tissue scaffolds implanted in cartilage *Tissue Eng.* C **20** 140–8
[28] Nie X, Chuah Y J, Zhu W, He P, Peck Y and Wang D-A 2020 Decellularized tissue engineered hyaline cartilage graft for articular cartilage repair *Biomaterials* **235** 119821
[29] Martinez-Diaz S *et al* 2010 In vivo evaluation of 3-dimensional polycaprolactone scaffolds for cartilage repair in rabbits *Am. J. Sports Med.* **38** 509–19
[30] Olubamiji A D, Zhu N, Chang T, Nwankwo C K, Izadifar Z, Honaramooz A, Chen X and Eames B F 2017 Traditional invasive and synchrotron-based noninvasive assessments of three-dimensional-printed hybrid cartilage constructs in situ *Tissue Eng.* C **23** 156–68
[31] Cartmell S, Huynh K, Lin A, Nagaraja S and Guldberg R 2004 Quantitative microcomputed tomography analysis of mineralization within three-dimensional scaffolds *in vitro J. Biomed. Mater. Res.* A **69** 97–104
[32] Izadifar Z, Honaramooz A, Wiebe S, Belev G, Chen X and Chapman D 2016 Low-dose phase-based x-ray imaging techniques for in situ soft tissue engineering assessments *Biomaterials* **82** 151–67
[33] Nitzsche H, Metz H, Lochmann A, Bernstein A, Hause G, Groth T and Mäder K 2009 Characterization of scaffolds for tissue engineering by benchtop-magnetic resonance imaging *Tissue Eng.* C **15** 513–21
[34] van Lenthe G H, Hagenmüller H, Bohner M, Hollister S J, Meinel L and Müller R 2007 Nondestructive micro-computed tomography for biological imaging and quantification of scaffold–bone interaction in vivo *Biomaterials* **28** 2479–90
[35] Prang P, Müller R, Eljaouhari A, Heckmann K, Kunz W, Weber T, Faber C, Vroemen M, Bogdahn U and Weidner N 2006 The promotion of oriented axonal regrowth in the injured spinal cord by alginate-based anisotropic capillary hydrogels *Biomaterials* **27** 3560–9
[36] Zehbe R, Haibel A, Riesemeier H, Gross U, Kirkpatrick C J, Schubert H and Brochhausen C 2010 Going beyond histology. Synchrotron micro-computed tomography as a methodology for biological tissue characterization: from tissue morphology to individual cells *J. R. Soc. Interface* **7** 49–59
[37] Gabor D 1948 A new microscopi prinnciple *Nature* **161** 777–8
[38] Wilkins S, Gureyev T E, Gao D, Pogany A and Stevenson A 1996 Phase-contrast imaging using polychromatic hard x-rays *Nature* **384** 335–8
[39] Olubamiji A D, Izadifar Z and Chen D X 2014 Synchrotron imaging techniques for bone and cartilage tissue engineering: potential, current trends, and future directions *Tissue Eng.* B **20** 503–22
[40] Spanne P, Raven C, Snigireva I and Snigirev A 1999 In-line holography and phase-contrast microtomography with high energy x-rays *Phys. Med. Biol.* **44** 741
[41] Ning L *et al* 2021 Noninvasive three-dimensional in situ and in vivo characterization of bioprinted hydrogel scaffolds using the x-ray propagation-based imaging technique *ACS Appl. Mater. Interfaces* **13** 25611–23
[42] Bhartiya A *et al* 2020 Phase-contrast 3D tomography of HeLa cells grown in PLLA polymer electrospun scaffolds using synchrotron x-rays *J. Synchrotron Radiat.* **27** 158–63
[43] Yao Y and Wang Y 2013 ATDC5: an excellent *in vitro* model cell line for skeletal development *J. Cell Biochem.* **114** 1223–9
[44] Alizadeh Sardroud H, Chen X and Eames B F 2023 Applied compressive strain governs hyaline-like cartilage versus fibrocartilage-like ECM produced within hydrogel constructs *Int. J. Mol. Sci.* **24** 7410
[45] Frisbie D, Cross M and McIlwraith C 2006 A comparative study of articular cartilage thickness in the stifle of animal species used in human pre-clinical studies compared to articular cartilage thickness in the human knee *Vet. Comp. Orthop. Traumatol.* **19** 142–6
[46] Sardroud H A, Wanlin T, Chen X and Eames B F 2021 Cartilage tissue engineering approaches need to assess fibrocartilage when hydrogel constructs are mechanically loaded *Front. Bioeng. Biotechnol.* **9** 787538
[47] Meng X, Ziadlou R, Grad S, Alini M, Wen C, Lai Y, Qin L, Zhao Y and Wang X 2020 Animal models of osteochondral defect for testing biomaterials *Biochem. Res. Int.* **2020** 1–12
[48] Siclari A, Mascaro G, Gentili C, Cancedda R and Boux E 2012 A cell-free scaffold-based cartilage repair provides improved function hyaline-like repair at one year *Clin. Orthop. Relat. Res.* **470** 910–9
[49] Wayne J S, McDowell C L, Shields K J and Tuan R S 2005 In vivo response of polylactic acid–alginate scaffolds and bone marrow-derived cells for cartilage tissue engineering *Tissue Eng.* **11** 953–63
[50] Lösel P D *et al* 2020 Introducing Biomedisa as an open-source online platform for biomedical image segmentation *Nat. Commun.* **11** 1–14
[51] McManus J F A and Mowry R W 1960 *Staining Methods: Histologic and Histochemical* (Paul B. Hoeber)
[52] Ashique A M, Atake O J, Ovens K, Guo R, Pratt I V, Detrich H W III, Cooper D M L, Desvignes T, Postlethwait J H and Eames B F 2022 Bone microstructure and bone mineral density are not systemically different in Antarctic icefishes and related Antarctic notothenioids *J. Anat.* **240** 34–49
[53] Hyllested J, Veje K and Ostergaard K 2002 Histochemical studies of the extracellular matrix of human articular cartilage—a review *Osteoarthritis Cartilage* **10** 333–43
[54] Benjamin M, Kumai T, Milz S, Boszczyk B, Boszczyk A A and Ralphs J R 2002 The skeletal attachment of tendons—tendon 'entheses' *Comp. Biochem. Physiol.* A **133** 931–45
[55] Alizadeh Sardroud H, Chen X and Eames B F 2023 Reinforcement of hydrogels with a 3D-Printed polycaprolactone (PCL) structure enhances cell numbers

and cartilage ECM production under compression *J. Funct. Biomater.* **14** 313
[56] Dahab G M, Kheriza M M, El-beltagi H M, Fouda A M M and El-din O A S 2004 Digital quantification of fibrosis in liver biopsy sections: description of a new method by Photoshop software *J. Gastroenterol. Hepatol.* **19** 78–85
[57] Wang X, Xue Y, Ye W, Pang J, Liu Z, Cao Y, Zheng Y and Ding D 2018 The MEK-ERK1/2 signaling pathway regulates hyaline cartilage formation and the redifferentiation of dedifferentiated chondrocytes *in vitro Am. J. Transl. Res.* **10** 3068
[58] Alcaide-Ruggiero L, Molina-Hernández V, Granados M M and Domínguez J M 2021 Main and minor types of collagens in the articular cartilage: the role of collagens in repair tissue evaluation in chondral defects *Int. J. Mol. Sci.* **22** 13329
[59] Mayo S C, Stevenson A W and Wilkins S W 2012 In-line phase-contrast x-ray imaging and tomography for materials science *Materials* **5** 937–65
[60] Mhanna R, Kashyap A, Palazzolo G, Vallmajo-Martin Q, Becher J, Möller S, Schnabelrauch M and Zenobi-Wong M 2014 Chondrocyte culture in three dimensional alginate sulfate hydrogels promotes proliferation while maintaining expression of chondrogenic markers *Tissue Eng.* A **20** 1454–64
[61] Koo Y, Choi E-J, Lee J, Kim H-J, Kim G and Do S H 2018 3D printed cell-laden collagen and hybrid scaffolds for in vivo articular cartilage tissue regeneration *J. Ind. Eng. Chem.* **66** 343–55
[62] Lotz B *et al* 2021 Preclinical testing of new hydrogel materials for cartilage repair: overcoming fixation issues in a large animal model *Int. J. Biomater.* **2021** 1–14
[63] Bothe F, Deubel A-K, Hesse E, Lotz B, Groll J, Werner C, Richter W and Hagmann S 2019 Treatment of focal cartilage defects in minipigs with zonal chondrocyte/mesenchymal progenitor cell constructs *Int. J. Mol. Sci.* **20** 653
[64] Woodruff M A and Hutmacher D W 2010 The return of a forgotten polymer—polycaprolactone in the 21st century *Prog. Polym. Sci.* **35** 1217–56
[65] Distler T, Schaller E, Steinmann P, Boccaccini A and Budday S 2020 Alginate-based hydrogels show the same complex mechanical behavior as brain tissue *J. Mech. Behav. Biomed. Mater.* **111** 103979
[66] Lee H-P, Gu L, Mooney D J, Levenston M E and Chaudhuri O 2017 Mechanical confinement regulates cartilage matrix formation by chondrocytes *Nat. Mater.* **16** 1243–51
[67] Garrity C, Arzi B, Haus B, Lee C A and Vapniarsky N 2022 A fresh glimpse into cartilage immune privilege *Cartilage* **13** 119–32
[68] Steadman J, Rodkey W, Briggs K and Rodrigo J 1999 The microfracture technique to treat full thickness articular cartilage defects of the knee *Der Orthop.* **28** 26–32
[69] Schulz G, Barbero A, Wolf F, Rodgers G, Tanner C, Weitkamp T, Mumme M, Morawska M, Beer D and Müller B 2022 Three-dimensional imaging of porcine joint tissues down to the subcellular level (arXiv:2211.08965)
[70] Hesse B *et al* 2015 Canalicular network morphology is the major determinant of the spatial distribution of mass density in human bone tissue: evidence by means of synchrotron radiation phase-contrast nano-CT *J. Bone Miner. Res.* **30** 346–56
[71] Soares da Costa D, Reis R L and Pashkuleva I 2017 Sulfation of glycosaminoglycans and its implications in human health and disorders *Annu. Rev. Biomed. Eng.* **19** 1–26
[72] Duan X, Chen X and Zhu N 2023 A strategy to improve image quality of low-dose synchrotron radiation CT imaging for tissue engineering applications *CMBES Proc.* vol 45
[73] Thomlinson W, Elleaume H, Porra L and Suortti P 2018 K-edge subtraction synchrotron x-ray imaging in bio-medical research *Phys. Med.* **49** 58–76